SCIENCE CHINA
Information Sciences

• RESEARCH PAPER •

April 2026, Vol. 69, Iss. 4, 142405:1–142405:12
https://doi.org/10.1007/s11432-025-4674-2

Robust optoelectronic dual-mode memristor enabled by ZnO/MoS_2 heterojunction for synaptic bionics and in-memory computing

Xiaoyan LIU[1,4], Youshan GUI[1], Zhou WANG[1,4*], Pengcheng ZHOU[1], Junyuan CHEN[1], Tenglong GUO[1], Xin ZHANG[1], Suo ZHANG[1], Xian WEI[3], Jin WANG[3], Xiaojuan LIAN[1,4], Xiang WAN[1,4], Nan HE[1,4], Yan GU[1,4], Er-Tao HU[3], Qiang CHEN[1], Haifeng LING[2,4*] & Lei WANG[1,4*]

[1]*College of Integrated Circuit Science and Engineering, Nanjing University of Posts and Telecommunications, Nanjing 210023, China*
[2]*State Key Laboratory of Flexible Electronics (LoFE) & Institute of Advanced Materials (IAM), Nanjing University of Posts and Telecommunication, Nanjing 210023, China*
[3]*College of Electronic and Optical Engineering, Nanjing University of Posts and Telecommunications, Nanjing 210023, China*
[4]*Jiangsu Key Laboratory of Neuromorphic Electronic Materials and Devices, Nanjing University of Posts and Telecommunications, Nanjing 210023, China*

Received 2 June 2025/Revised 2 August 2025/Accepted 5 November 2025/Published online 11 February 2026

Abstract The current von Neumann computing architecture based on traditional complementary metal oxide semiconductor (CMOS) transistors, which separates memory from process units, faces severe challenges of insufficient computing capability and high power consumption in artificial intelligence. To address these key bottlenecks, memristor-enabled neuromorphic computing has emerged as a promising solution. Herein, an optoelectronic dual-mode memristor based on a ZnO/MoS_2-heterojunction featuring tunable characteristics through interface engineering has been proposed. By applying different types of electrical and optical signals, the device successfully emulates synaptic plasticity including paired-pulse facilitation, long-term potentiation and long-term depression. Besides, the MoS_2 insertion layer significantly enhances the stability and uniformity of the memristor, achieving 580-cycle resistive switching with over 10^4 s retention time and low coefficient of variation of 18.30% for the high resistance state and 7.26% for the low resistance state, indicating excellent operational reliability. Furthermore, we employed SPICE simulations to implement memristor-based AND, OR, and NOT logic circuits. At the same time, a convolutional neural network for handwritten digit recognition is constructed, reaching 99% recognition accuracy. In addition, a biomimetic artificial visual system is implemented using a 3×3 ZnO/MoS_2 memristor array. Therefore, the optoelectronic memristor developed in this work provides a viable solution to promote the development of next-generation in-memory and neuromorphic computing.

Keywords optoelectronic memristor, ZnO-MoS_2 heterojunction, reliability, neuromorphic computing, artificial visual system

Citation Liu X Y, Gui Y S, Wang Z, et al. Robust optoelectronic dual-mode memristor enabled by ZnO/MoS_2 heterojunction for synaptic bionics and in-memory computing. Sci China Inf Sci, 2026, 69(4): 142405, https://doi.org/10.1007/s11432-025-4674-2

1 Introduction

The rapid development of the Internet of Things (IoT), big data, and artificial intelligence (AI) has exposed limitations in traditional memory and computing technologies based on von Neumann architectures due to the separated storage and computation units, particularly in terms of energy efficiency, processing speed, and integration density. These challenges have driven considerable research efforts toward novel computing paradigms, with memristor emerging as a promising solution. Memristors demonstrate the inherent ability to store and process information in a single device endowed with unique in-memory computing capabilities, making them a promising candidate for next-generation storage and computing technologies. Compared to conventional complementary metal oxide semiconductor (CMOS)-based transistors, memristors exhibit lower power consumption, higher speeds, and greater integration density [1–7]. What is more noteworthy is that their dynamic conductance modulation mimics biological synaptic plasticity, enabling the implementation of brain-inspired neuromorphic computing architectures. The superior resistive-switching characteristics and biomimetic functionality have facilitated widespread applications

* Corresponding author (email: zhouwang@njupt.edu.cn, iamhfling@njupt.edu.cn, leiwang1980@njupt.edu.cn)

of the memristors in high-density non-volatile memory, neuromorphic computing, adaptive edge computing, and reconfigurable radio frequency communications [4, 8–19].

Various metal oxides (e.g., ZnO, TiO_2, HfO_2) are used in memristive synapses due to their resistive switching characteristics [20–22]. ZnO, a wide-bandgap (3.3 eV) semiconductor, offers high stability, speed, and energy efficiency, while its light response facilitates optical modulation for neuromorphic visual networks [23–25]. Therefore, great progress has been made in ZnO memristors; however, critical challenges persist including reliability, durability, retention characteristics, power consumption, multimodal stimulus-driven sensor-memory-computing integration (e.g., optoelectronic dual-mode), controllable conductive filament formation/rupture, broadband photoresponse range, and CMOS compatibility. As a representative strategy, the construction of heterojunction structures not only effectively suppresses the recombination of photoexcited carriers but also inhibits the overgrowth of conductive filaments (CFs), enabled by tunable interfacial properties via synergistic modulation of material interfaces in engineered heterojunction architectures [26–33]. Xu et al. developed a flexible N:ZnO/MoS_2 heterojunction optoelectronic synapse on mica substrates, mimicking synaptic plasticity (e.g., long-term potentiation (LTP), long-term depression (LTD) and paired-pulse facilitation (PPF)) and adaptive learning-forgetting-relearning behavior under tunable light stimuli [33]. However, unlike memristive devices, it lacks non-volatile memory capability, necessitating sustained external inputs for memory retention and limiting standalone storage applications. Lin et al. developed a full-quantum-dot optoelectronic memristor (FQDOM) based on a ZnO/CdSe/ZnO heterojunction, which exhibited broadband spectral response, color perception, and multisensory fusion, achieving 92.59% accuracy in dynamic gesture recognition [27]. Its solution-processed fabrication involving sequential spin-coating of colloidal quantum dots and low-temperature annealing is inherently incompatible with CMOS technology. Although ZnO-heterostructured memristors have been extensively reported, the MoS_2/ZnO heterojunction memristors for synaptic bionics and in-memory computing applications remain notably unexplored. A study on interfacial engineering in Ag/ZrO_2/MoS_2/Pt memristor discovered that the insertion of the MoS_2 layer could significantly eliminate the unexpected negative-SET behavior. This is because the ionic blocking of MoS_2 prevents the formation of uncontrolled CFs, confirming that the MoS_2 layer can improve the performance of memristors [34]. Another advantage is that the ZnO/MoS_2 heterojunction was proven to exhibit exceptional broadband photoresponse from ultraviolet to visible light [35–37]. These characteristics enable the implementation of optoelectronic memristors capable of multimodal artificial synapses under optical-electrical dual-mode operation.

Motivated by these considerations, we successfully fabricated an optoelectronic dual-mode memristor with the structure TiN/Ag/ZnO/MoS_2/Pt (referred to as ZnO/MoS_2 memristor) in this study. Devices without the MoS_2 layer, having the structure TiN/Ag/ZnO/Pt (referred to as ZnO memristor), encountered the issue of negative-SET behavior. The MoS_2 layer effectively resolved this issue, resulting in improved stability, longer retention time, lower switching voltage, better device-to-device uniformity, and faster response time. Based on experimental data, we utilized SPICE to develop logic circuits based on ZnO/MoS_2 memristors. To elucidate the working mechanism of the ZnO/MoS_2 memristor, we fitted its current-voltage (I-V) characteristics, revealing a combined space-charge-limited current (SCLC) mechanism. Additionally, first-principles calculations demonstrated that the MoS_2 layer acts as a barrier, preventing Ag ions (Ag^+) from entering the bottom electrode (Pt), thus suppressing the excessive growth of CFs under negative voltage and enhancing device stability. Moreover, the device exhibits excellent synaptic plasticity under both electrical and optical stimuli, such as excitatory postsynaptic current (EPSC), PPF, LTP, and LTD. Leveraging its opto-synaptic plasticity, we implemented a convolutional neural network (CNN) for handwritten digit recognition, achieving an accuracy of up to 99%. Finally, we simulated a biological visual perception system using a 3×3 memristor array. This work makes significant contributions to the development of artificial synaptic devices and optoelectronic-operated bioinspired visual systems.

2 Results and discussion

The structure and properties of our device were comprehensively analyzed through a combination of morphological, elemental, and optical characterization techniques. As illustrated in Figure 1(a), the device was fabricated on a Si substrate with a multilayer configuration of TiN/Ag/ZnO/MoS_2/Pt. The TiN layer protected Ag from oxidation, while the ZnO and MoS_2 layers served as the functional materials. Scanning electron microscope (SEM) images shown in Figures 1(b) and (c) illustrate the surface morphology of the MoS_2 and ZnO thin films, respectively. Both films exhibited nanograin structures, whereas ZnO displayed relatively larger grain sizes compared to MoS_2. Randomly selected SEM images demonstrate uniform film growth across the substrate, which is critical for enhancing device performance. Furthermore, the cross-sectional SEM image in Figure 1(d) clearly presents the well-defined layering of the heterostructure, with thicknesses of approximately 10 nm for the MoS_2 layer, 60 nm for

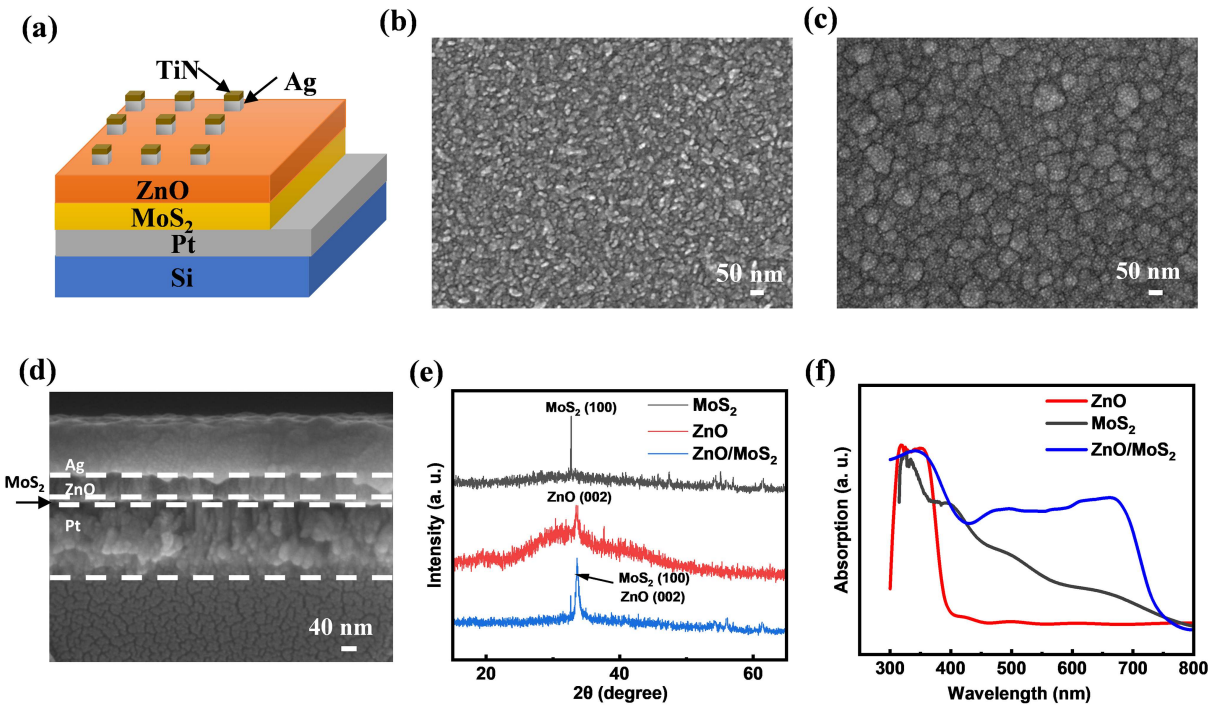

Figure 1 (Color online) (a) Schematic diagram of the memristor structure; surface SEM images of (b) MoS_2 and (c) ZnO thin films; (d) cross-section SEM image of the ZnO/MoS_2 memristor; (e) XRD patterns of MoS_2, ZnO and ZnO/MoS_2 thin films; (f) absorption spectra of MoS_2, ZnO and ZnO/MoS_2 thin films.

the ZnO layer, and 100 nm for both the Pt and Ag layers. The distinct boundaries between layers highlight the high-quality deposition and structural integrity of the device. Elemental analysis through energy-dispersive X-ray spectroscopy (EDS), as illustrated in Figure S1, verifies the successful deposition of each layer. The identified peaks corresponding to Zn, O, Mo, S, Pt, Ag, Ti, and N confirm the presence of ZnO, MoS_2, Pt, Ag, and TiN in the heterostructure. Additionally, X-ray diffraction (XRD) patterns (Figure 1(e)) display the crystallographic orientation of the films. Specifically, the ZnO film exhibited a predominant (002) peak, while the MoS_2 film displayed a characteristic (100) peak, indicating the crystalline nature of both materials. The XRD spectrum of the ZnO/MoS_2 heterostructure further confirms the successful integration of these materials. As depicted in Figure 1(f), optical absorption measurements revealed that the ZnO film had a strong absorption peak in the ultraviolet (UV) region (300–400 nm). Notably, the ZnO/MoS_2 heterostructure demonstrated enhanced absorption across a wider wavelength range (300–700 nm), suggesting that the inclusion of MoS_2 broadens the light absorption spectrum, a feature beneficial for optoelectronic applications. Furthermore, the ZnO/MoS_2 film exhibited stronger optical absorption in the visible light region compared to the MoS_2 film, a property that may result from the formation of interface states and a reduced interface bandgap [38]. The transmittance spectra shown in Figure S2 indicate that the ZnO film achieved higher transmittance than the MoS_2 film in visible light. Consequently, the heterojunction of ZnO/MoS_2 is engineered to allow visible light to pass through ZnO and subsequent absorption by MoS_2, thereby extending absorption into both UV and visible regions, ultimately enabling broadband white-light response capability. Besides, to elucidate the interaction between the incident light and the ZnO/MoS_2 functional layer, the optical transmission spectrum of the TiN/Ag top electrode and the optical power densities before and after passing through the top electrode were measured, as shown in Figure S3.

The memristor underwent repeated cyclic electrical testing to comprehensively evaluate its reliability and performance under direct current (DC) voltage sweep mode. As a comparison, the electrical property of the ZnO memristor was first measured shown in Figure 2(a). The device initially exhibited a high resistance state (HRS) with a resistance of approximately 10^3 Ω, measured at a read voltage of 0.05 V. Upon applying a positive voltage sweep (0 to 2.5 V) to the Ag electrode, the device transitioned from HRS to a low resistance state (LRS), with the resistance decreasing to approximately 42 Ω at the SET voltage of about 1.45 V. However, during a negative voltage sweep (0 to −1.5 V), a negative-SET behavior occurred, where the resistance initially increased slightly at −0.62 V before experiencing a rapid decrease, indicating a RESET failure. Figure 2(b) depicts the typical DC I-V characteristic curves of the ZnO/MoS_2 heterojunction memristor with a compliance current (I_{CC}) of 10 mA in logarithmic coordinates. It can be seen that the ZnO/MoS_2 memristor demonstrated typical bipolar RS characteristics. By

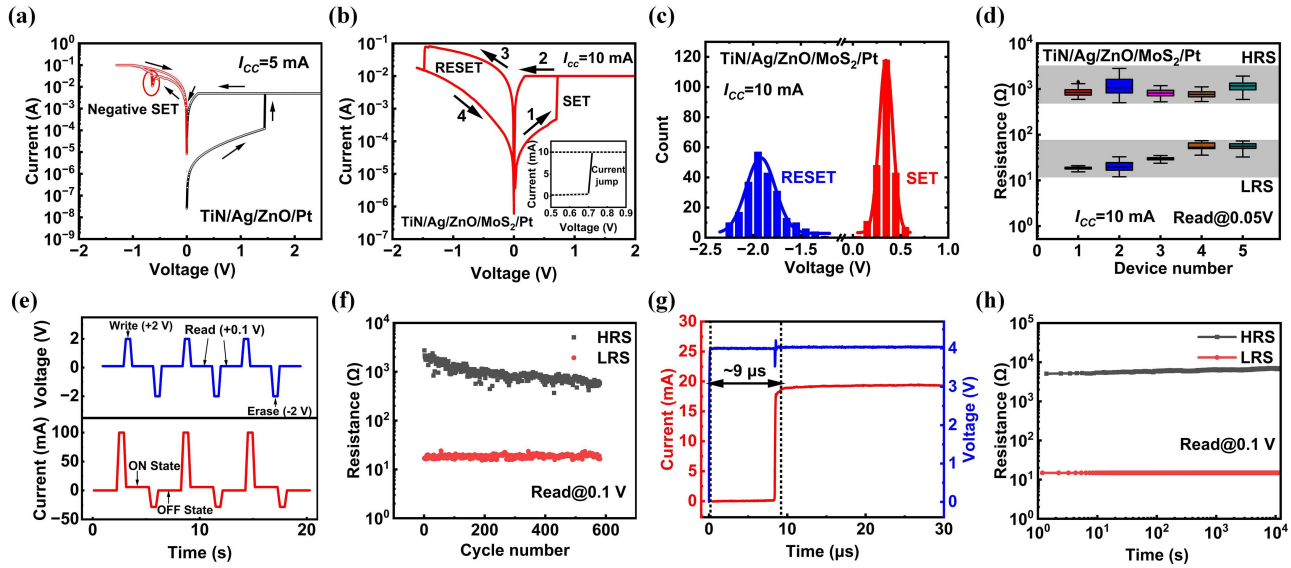

Figure 2 (Color online) Electrical resistance switching characteristics of memristors under DC sweep mode. The representative I-V characteristics of (a) ZnO memristor and (b) ZnO/MoS_2 memristor under logarithmic coordinates. Inset: the ZnO/MoS_2 memristor shows a switching slope of less than 9.44 mV/dec. (c) Distributions of V_{set} and V_{reset} for 220 cycles. (d) Resistance distributions of HRS and LRS for five different devices. Electrical resistance switching characteristics of ZnO/MoS_2 memristors in pulse mode. (e) I-V characteristics of the ZnO/MoS_2 memristor with a Write pulse of 2 V and an Erase pulse of −2 V. (f) Endurance characteristics of HRS and LRS for more than 500 cycles with a Write pulse of 2 V and an Erase pulse of −2 V. Both of the pulse widths of the Write and Erase pulses are 0.4 s. (g) Measurement of SET switching time. (h) Retention performance of the HRS and LRS for ZnO/MoS_2 memristor.

sweeping the bias voltage (0 V → 1.5 V → −1.6 V → 0 V), the ZnO/MoS_2 memristor switched from HRS to LRS at the SET voltage (V_{set}) and returned from LRS to HRS at the RESET voltage (V_{reset}). The sharp switching slope of the SET operation (∼9.44 mV/dec seen from the inset of Figure 2(b)) is particularly advantageous for array-level operations, enabling a large read voltage margin and fast read speeds. The I-V curves in Figure 2(b) were plotted and analyzed on a linear scale for fitting to explore the conduction mechanisms of the ZnO/MoS_2 memristor, as shown in Figure S4. Analysis of the I-V characteristics reveals distinct conduction mechanisms. The HRS was dominated by the SCLC mechanism, whereas LRS followed Ohmic conduction, as evidenced by the excellent agreement between experimental data and theoretical models. Electrode size-independent LRS resistance (Figure S5) further confirmed CF-dominated transport [39]. The detailed analysis is shown in Supporting Information (Appendix A). To quantify the operational stability, the statistical distribution of V_{set} and V_{reset} was systematically investigated. Figure 2(c) depicts the V_{set} and V_{reset} distribution, followed by a Gaussian distribution centered at approximately 0.35 and −1.92 V, respectively. It indicates that the improved ZnO/MoS_2 memristor demonstrated superior cycle-to-cycle repeatability and high stability compared to the ZnO memristor. To further evaluate the reliability of the ZnO/MoS_2 memristor, five different devices fabricated on the same wafer were tested for device-to-device variation. The boxplot of the resistance distribution (Figure 2(d)) and the cumulative probability plot of V_{set} for five devices (Figure S6) exhibited minimal variation across devices. The endurance of the device was evaluated by performing repeated DC sweeps under I_{CC} = 10 mA for 220 cycles. Figure S7(a) presents the resistance distribution of HRS and LRS across these cycles, demonstrating a stable on/off ratio of approximately 26. The cumulative probability of the HRS and LRS resistance for 220 cycles, shown in Figure S7(b), indicated mean resistance values of 787.18 and 29.73 Ω, respectively. The corresponding coefficients of variation, defined as the ratio of standard deviation (σ) to arithmetic mean (μ), were calculated to be 18.30% and 7.26%, respectively, which is at a low level in ZnO-based memristors (shown in Table S1). These findings validate the potential for scalable and reproducible fabrication of ZnO/MoS_2 memristors, confirming their suitability for practical applications.

In operational circuit implementations, pulses are commonly employed to set or reset memristors for state programming. As a result, the pulse-switching characteristics of the ZnO/MoS_2 memristor were systematically characterized in Figures 2(e)–(h). Figure 2(e) demonstrates the cyclic endurance of the ZnO/MoS_2 memristor under a sequence of voltage pulses. The applied pulse voltage (denoted by the blue line) consisted of alternating operational cycles: a 'Write' pulse with an amplitude of +2 V and a pulse width of 0.4 s to establish the LRS, followed by an 'Erase' pulse of −2 V with identical 0.4 s duration to facilitate HRS recovery. The corresponding response current (denoted by the red line) reflects the change in resistance, with lower currents indicating the HRS and higher currents representing the LRS. Following each 'Write' and 'Erase' operation, a 'Read' pulse of 0.1 V with a

pulse width of 2.2 s was applied to verify the non-destructive readout characteristics due to the minor perturbation in current, which indicates the stability of the memristive state during read operations. The endurance of HRS and LRS after 580 pulse cycles is depicted in Figure 2(f), confirming the ability of the ZnO/MoS_2 memristor to maintain distinct resistance states. The concentration of data points within each resistance state suggests a low variability in resistance levels, which is indicative of stable pulse-switching characteristics. Figure 2(g) and Figure S8 show the switching times for the Write and Erase processes of the ZnO/MoS_2 memristor, which were 9 and 6.2 μs, respectively. Furthermore, the device exhibited robust data retention, exceeding 10^4 s, as shown in Figure 2(h). The evidence presented by the results demonstrates the viability of ZnO/MoS_2 memristors as robust binary switches in computing applications, bolstering their prospect for integration into future memory and logic architectures.

According to the above experimental results, the switching mechanism of the ZnO/MoS_2 memristor and the role of MoS_2 in enhancing its endurance are depicted in Figure 3. For the ZnO memristor, applying a positive voltage on the Ag electrode initiates the oxidation of Ag atoms, producing Ag^+. These Ag^+ migrate under the influence of the electric field and are subsequently reduced to Ag atoms over a short migration distance. This process results in the formation of Ag CF stretching from the Ag to the Pt electrodes, as shown in Figure 3(b). It can be seen that these CFs tend to extend into the Pt electrode due to the low diffusion barrier for Ag ions/atoms. During the negative-RESET process, thermal-assisted electrochemical reactions partially rupture the Ag CF near the Pt electrode, specifically at the CF's bottleneck, as demonstrated in Figure 3(c). Upon applying a higher negative voltage, Ag precipitation at the Pt electrode acts as a localized anode, releasing Ag^+ into the ZnO layer. These ions predominantly migrate towards the tip of the residual CF, where the electric field is strongest within the ZnO layer. When sufficient Ag^+ is reduced back to Ag atoms in the gap, the CF reconnects to the Pt electrode, leading to a return to LRS, causing a RESET failure, as displayed in Figure 3(d). However, the introduction of MoS_2 in ZnO/MoS_2 heterojunction as a barrier layer at the top of the Pt electrode modifies the dynamics of ion transport and CF formation. The ion barrier effect and low thermal conductivity of MoS_2 suppress the penetration of Ag^+ into the Pt electrode. This effectively reduces the conflicting mechanisms of CF growth and dissolution, thereby preventing the occurrence of RESET failures, as illustrated in Figures 3(e) and (f) [34].

To further support our hypothesis, we conducted first-principles calculations to evaluate the energy barriers associated with Ag^+ migration through ZnO/Pt and MoS_2/Pt interfaces (computational details seen from Appendix B in Supporting Information). Optimized structural configurations for the ZnO/Pt and MoS_2/Pt contacts are exhibited in Figures S9(a) and (b). Figure S9(c) presents that Ag^+ migrates within the ZnO layer via atomic interstitial sites until reaching the ZnO/Pt interface, with the maximum energy barrier measured at 1.40 eV, as shown in Figure S9(d). The pathway and energy barrier for Ag^+ migrating from the ZnO/Pt interface into the Pt layer are illustrated in Figures S9(e) and (f), with a maximum barrier of 2.29 eV. Therefore, the cumulative energy barrier for Ag^+ migration from ZnO into Pt is calculated to be 3.69 eV. In contrast, assume that Ag^+ migration within the MoS_2 layer is restricted. Migration necessitates the displacement of Mo atoms to create vacancies, which then allows Ag^+ mobility through MoS_2, as displayed in Figure 3(g). The energy barrier associated with Ag^+ migration within MoS_2 is shown in Figure 3(i), reaching a maximum of 6.31 eV. The migration pathway and corresponding energy barrier for Ag^+ moving from the MoS_2/Pt interface into the Pt layer are demonstrated in Figures 3(h) and (j), with a maximum barrier of 3.15 eV. Consequently, the total energy barrier for Ag^+ migration through MoS_2 into Pt is determined to be 9.46 eV, significantly greater than the barrier for Ag^+ migration through ZnO into Pt. These findings confirm that the insertion of MoS_2 acts as an effective barrier layer, effectively mitigating the uncontrolled growth of Ag CFs within the device.

To further explore the in-memory computing application of the ZnO/MoS_2 memristor, the simulation of logic circuits based on experimental data from memristors is illustrated in Figure 4. Figures 4(a), (c) and (e) present the circuit diagrams for the AND, OR, and NOT gates, respectively. The corresponding simulated outputs for different binary input combinations (0 and 1) are illustrated in Figures 4(b), (d), (f). In the simulations, the HRS of the memristor was mapped to logic 0, whereas the LRS corresponds to logic 1. For both AND and OR gates, the operation consisted of two phases controlled by a clock signal. The first phase was the initialization phase, during which the switch remains open, setting the input memristors R_{M1} and R_{M2} to either 0 (HRS) or 1 (LRS) while initializing the output memristor R_{MO} to 0 (HRS). In the second phase, the switch was closed, and the circuit was connected to the voltage source. In the AND gate circuit (Figure 4(a)), the two input memristors were connected in series. If either input memristor is in HRS, the voltage across R_{MO} is insufficient to transition R_{MO} to LRS, resulting in an output of 0. Only when both input memristors are in LRS does the voltage across R_{MO} become sufficient to induce a transition to LRS, producing a logic output of 1. In the OR gate circuit (Figure 4(c)), the two input memristors were connected in parallel. If at least one of the input memristors is in LRS, the voltage across R_{MO} is sufficient to switch it to the LRS, resulting in a logic output of 1. Conversely, if both input memristors

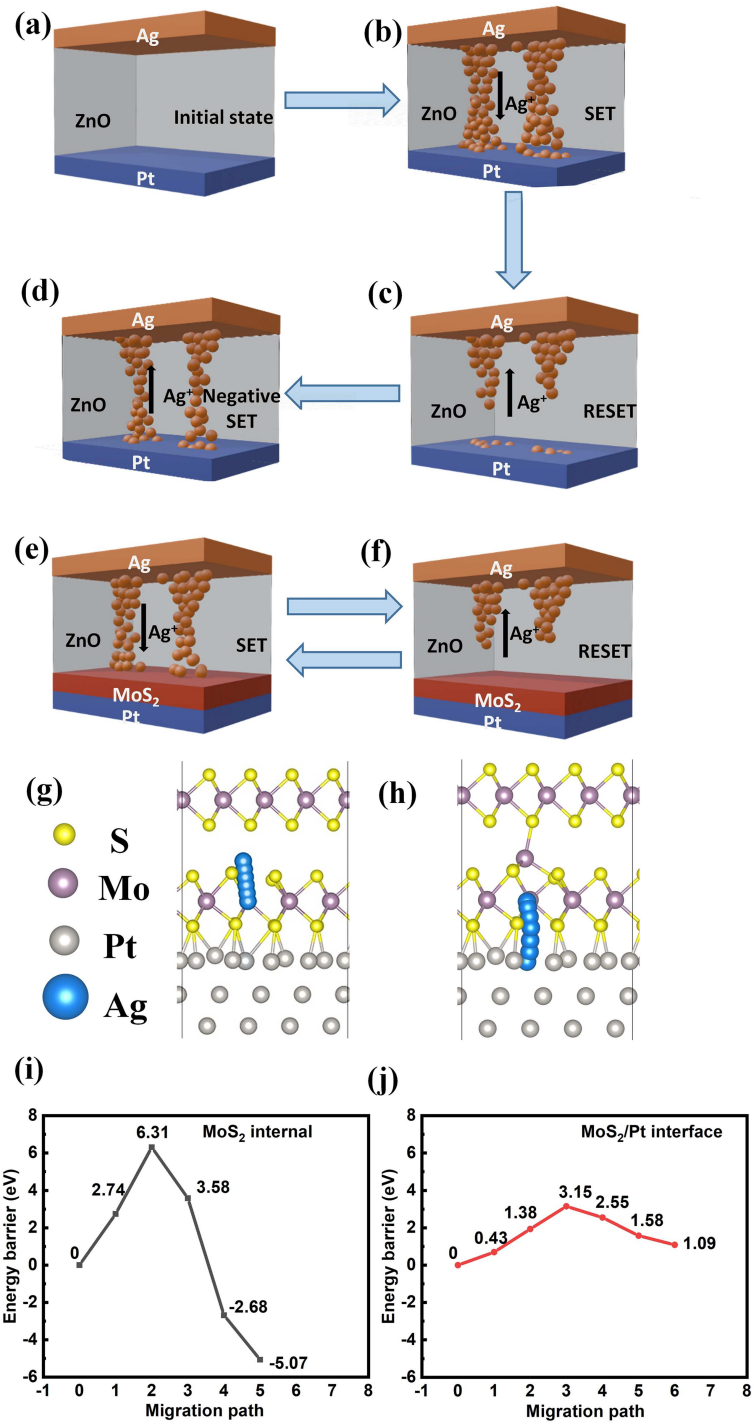

Figure 3 (Color online) Schematic illustrations of the switching mechanism of the ZnO memristor and the ZnO/MoS_2 memristor. (a) Initial state of the ZnO memristor. (b) Positive-SET process of the ZnO memristor. The CF forms in the ZnO layer and extends into the Pt electrode under the positive voltage. (c) Negative-RESET process of the ZnO memristor. The CF partially breaks near the Pt electrode while the Ag precipitation still remains in the Pt electrode. (d) Negative-SET process in ZnO memristor. The CF reconnects under a higher negative voltage due to the Ag precipitation in the Pt electrode, resulting in unexpected negative-SET behavior. (e) Positive-SET process of the ZnO/MoS_2 memristor. The CF does not extend into the Pt electrode due to the blocking effect of the MoS_2 layer. (f) Negative-RESET process of the ZnO/MoS_2 memristor. The CF ruptures near the Pt electrode without Ag precipitation, preventing the unexpected negative-SET behavior at negative voltages. (g) The migration path of Ag^+ inside MoS_2. (h) The migration path of Ag^+ on the MoS_2/Pt interface. Migration energy barrier of Ag^+ (i) inside MoS_2 and (j) at MoS_2/Pt interface.

are in HRS, the voltage across R_{MO} remains low, and the output remains 0. The NOT gate (Figure 4(e)) also operated in two phases. During the initialization phase, the input memristor was set to either 0 or 1, and the output

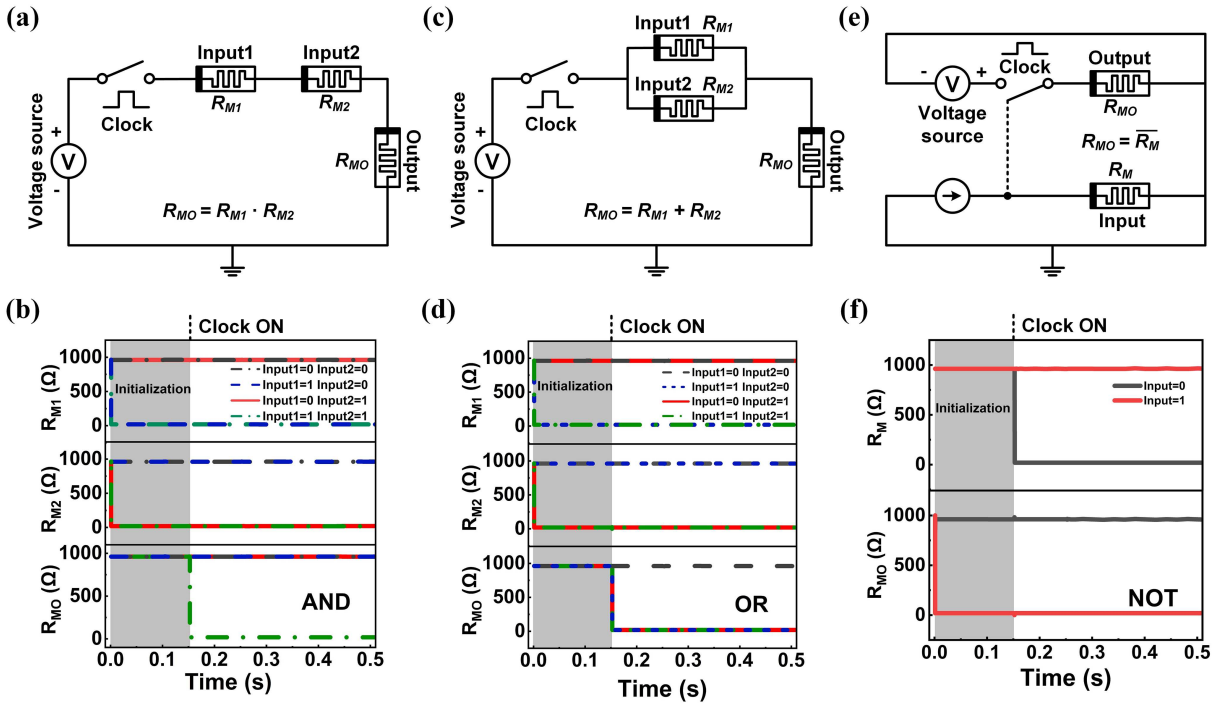

Figure 4 (Color online) (a) Schematic diagram and (b) simulation results of AND gate; (c) schematic diagram and (d) simulation results of OR gate; (e) schematic diagram and (f) simulation results of NOT gate.

memristor R_{MO} was initialized to 0 (HRS). In the second phase, the input memristor was connected to a current source, and the state of the switch depended on the bias voltage across the input memristor. When the input was 1, the voltage across the input memristor was low, keeping the switch open and R_{MO} in the high resistance state, producing a logic output of 0. Conversely, when the input was 0, the voltage across the input memristor was high, closing the switch, inducing a transition of R_{MO} to LRS, and producing an output of 1. Figures 4(b), (d), and (f) illustrate the simulated results for these gates based on different binary inputs.

The plasticity of the electrical synapse in the ZnO/MoS_2 memristor was investigated to explore its potential application in neuromorphic computing. Upon applying three consecutive positive voltage sweeps from 0 to 0.75 V, a current was observed to increase with each subsequent sweep (as shown in Figure 5(a)), mimicking the enhancement of synaptic weights through repeated stimulation. Conversely, when three consecutive negative voltages swept from 0 to −1.7 V were applied, a progressive decrease in current was observed (as presented in Figure 5(b)), simulating the suppression of synaptic weights. Therefore, the device effectively emulated the modulation of synaptic weights. Figure 5(c) illustrates the PPF index, which is a crucial metric for quantifying the facilitation effect in memristors exhibiting synaptic-like behaviors. The PPF index is defined as

$$\text{PPF} \quad \text{index} = \frac{I_2 - I_1}{I_1} \times 100\%, \tag{1}$$

where I_1 and I_2 represent the currents measured after the first and second voltage spike pulses, respectively. The decay curve of the PPF index with increased pulse intervals is accurately described by exponential fitting, aligning closely with the function,

$$\text{PPF} \quad \text{index} = y_0 + C\exp(-\Delta t/\tau), \tag{2}$$

where τ is the relaxation time, and C and y_0 are constants. This exponential fitting not only confirms the expected decrease in PPF with longer intervals but also provides quantitative insights into the synaptic-like response dynamics of the memristor. The excellent agreement between the model and experimental data demonstrates that the ZnO/MoS_2 memristor successfully emulates the intricate time-dependent behaviors of biological synapses. Figure 5(d) depicts the conductance update in the ZnO/MoS_2 memristor, tracked by applying 25 consecutive positive pulses (0.5 V) followed by 25 consecutive negative pulses (−0.5 V) with 0.05 s width and 0.05 s interval, simulating LTP and LTD characteristics analogous to those of biological synapses. It can be seen that under 25 positive pulse stimulation, the conductance progressively increased with pulse number increasing, then gradually slowed down and eventually saturated. This behavior corresponds to the LTP, wherein the resistance of the memristor decreases,

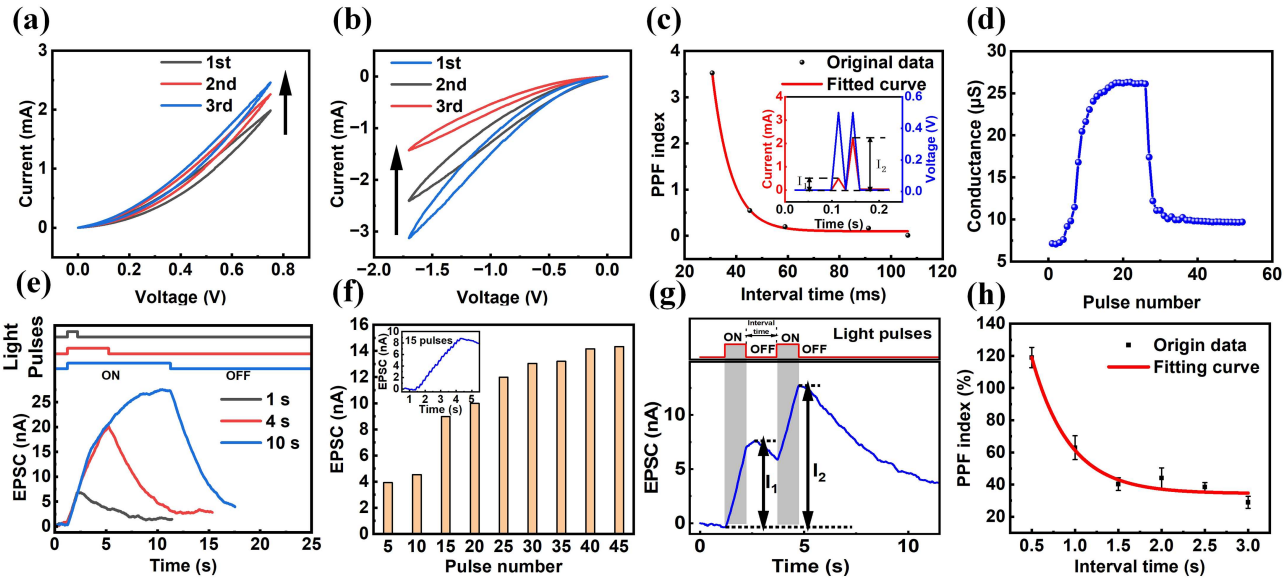

Figure 5 (Color online) Electrical and photonic synaptic behavior of the ZnO/MoS_2 memristor. Analog I-V characteristics of the memristor simulating synaptic weight modulation under (a) positive and (b) negative voltage sweeps. (c) The relationship between the PPF index and the electrical pulse interval. The inset is the current response of the memristor triggered by a pair of 0.5 V electrical spike pulses with 0.05 s pulse duration and 0.05 s pulse interval. (d) LTP and LTD characteristics of the device over 25 positive and 25 negative cycles pulses (amplitude = ±0.5 V, width = 0.05 s, and interval = 0.05 s). (e) EPSC evolution process with different durations of white-light irradiation. (f) EPSC of the ZnO/MoS_2 memristor with different numbers of light pulses. The inset is the EPSC with 15 light pulses. (g) EPSC of the ZnO/MoS_2 memristor triggered by a pair of lights with 1 s pulse duration and 1.5 s pulse interval. (h) The relationship between the PPF index and the light pulse interval.

enabling an increase in synaptic weight. Subsequently, 25 negative pulses were applied, causing a rapid decline in conductance, corresponding to the LTD, culminating in increased resistance and reduced synaptic weight. The above bidirectional conductance modulation indicates that the ZnO/MoS_2 memristor successfully replicated the electrical synaptic plasticity observed in biological systems, exhibiting both the strengthening and weakening of the connection between presynaptic and postsynaptic neurons, which are crucial for learning and memory processes in neural networks.

The ZnO/MoS_2 memristor also exhibited notable optical properties under zero voltage bias, with its photonic synaptic plasticity and neuromorphic computing functionalities systematically investigated under optical excitation, as illustrated in Figures 5(e) and (f). The high transmittance of the ZnO (Figure S2) enabled optimal photon penetration to the MoS_2 layer, thereby facilitating broadband spectral responsivity in the photonic synaptic behavior of the ZnO/MoS_2 memristor. As shown in Figure 5(e), the self-driven memristive device demonstrated synaptic behavior characterized by a transient increase followed by a gradual decline in the EPSC under varying durations of white-light exposure. The observed profiles for 1, 4, and 10 s light exposures indicate the implementation of short-term potentiation (STP) and LTP, analogous to biological synaptic functions. The immediate ascent in the current response emulates STP, where synaptic weight is transiently enhanced due to consecutive rapid stimuli, similar to the swift response under brief light exposure. As the light exposure duration extended, the device exhibited characteristics consistent with LTP, demonstrated by higher EPSC and slower decay following peak currents in EPSC. Based on the synaptic behavior observed under varying light durations, Figure 5(f) further examined the synaptic response as a function of the number of light pulses. It can be seen that the enhancement of synaptic response with increasing light pulses, as evident from the progressive increase in EPSC under the stimulus of 15 light pulses (inset in Figure 5(f)). This behavior aligns with the spike-number dependent plasticity (SNDP), validating the ability of the ZnO/MoS_2 memristor to emulate biological synaptic modulation in neural systems. Figure 5(g) illustrates the photonic PPF characteristic of the ZnO/MoS_2 memristor. When two identical light pulses with a duration time of 1 s and an interval time of 1.5 s were applied, an initial sharp increase in current was observed in response to the first pulse (I_1), followed by a higher peak corresponding to the second pulse (I_2), confirming the PPF behavior. The PPF index as a function of the interval time of the light pulse is presented in Figure 5(h) and aligns well with an exponential function. The fitting result is well in agreement with the experimental data, indicating that the light stimuli-induced PPF is also consistent with that observed in biological synapses, further supporting the memristor capability to simulate photonic synapses. These results underscore the potential of ZnO/MoS_2 memristors in neuromorphic engineering, particularly in developing photonic synaptic devices and

Table 1 Comparison of performance with other ZnO-based heterostructure memristors. NIMP represents not implies gate. IPSC represents inhibitory postsynaptic current. PPD represents paired-pulse depression.

Device structure	V_{set} (V)	V_{reset} (V)	Memory window	Cycle	Retention time (s)	Logic function	Electrical synaptic plasticity	Optical synaptic plasticity	Ref.
TiN/Ag/ZnO/MoS_2/Pt	0.35	−1.92	26	580	10^4	AND, OR, NOT	EPSC, PPF, LTP, LTD	EPSC, SNDP, PPF	This work
TiN/CeO_x /ZnO/ITO	∼ 7	∼ −7	∼ 10	–	–	–	–	LTP, SNDP	[19]
ITO/MoO_x /ZnO/W	–	–	–	–	–	AND, NOT, NIMP	–	EPSC, SNDP, PPF, LTP	[20]
ITO/ZnO QDs/CdSe QDs/ZnO QDs/Al	∼ 1	∼ −1	∼ 10^2	–	–	–	EPSC, SNDP, PPF	EPSC, IPSC, PPF, SNDP	[21]
Ni/p^+-Si/ n-ZnO/Ni	–	–	–	–	–	–	–	EPSC, IPSC, PPF, PPD, LTP, LTD	[22]
Al/N:ZnO/ MoS_2/ITO	–	–	–	–	–	–	LTP, LTD, PPF, PPD	EPSC, PPF, SNDP, Learning-Forgetting-Relearning	[27]

neural circuits capable of replicating the complex learning and memory dynamics observed in biological systems. The proposed mechanism is shown in Figure S10 and Appendix C in Supporting Information.

In the human visual system, optical information is initially detected and extracted by the retina, then propagated through the optic nerves, and ultimately processed in the visual cortex [40]. Inspired by this biological paradigm, a neuromorphic computing system integrating image sensing, preprocessing, and recognition functionalities was developed using ZnO/MoS_2 photonic synaptic arrays. These photonic synapses were designed to receive presynaptic spikes and temporarily store the corresponding information. Notably, the duration of this memory can be modulated through varying optical stimuli, thereby facilitating effective image preprocessing. As a consequence, to further explore the neuromorphic computing capabilities of ZnO/MoS_2 optoelectronic memristors, a 3-layer CNN was constructed based on these ZnO/MoS_2 photonic synapse arrays to evaluate their performance in image recognition tasks, specifically on the Modified National Institute of Standards and Technology (MNIST) handwritten digit dataset (28×28 pixels). The original image was preprocessed using the ZnO/MoS_2 memristor, and the resulting data were then fed into a CNN for recognition. Figure 6(a) presents a schematic diagram of the CNN architecture employed in the simulation, which comprises convolutional layers, pooling layers, fully connected layers, and activation functions. These components collectively enable the extraction of salient features from the input data, facilitating accurate classification. Figure 6(b) provides a comparison of the classification accuracy trends between the memristor-based CNN and an idealized software simulation over 40 training epochs. The memristor-based system achieved a classification accuracy of 94.98%, slightly lower than the 96.87% attained by the software-based model. Furthermore, the confusion matrix depicted in Figure 6(c) illustrates the recognition accuracy for each MNIST digit after 40 training epochs, with all digits achieving an accuracy above 88%, and a peak accuracy of 99%. These findings confirm the promising role of ZnO/MoS_2 memristors in emulating biological synaptic behavior and highlight their substantial potential for advancing neuromorphic computing applications. Figure 6(d) illustrates the implementation of a bioinspired proof-of-concept visual perception system based on ZnO/MoS_2 memristors. A 3×3 inverted T-shaped optical mask was placed over the device array during 15 s white-light exposure with an intensity through the top electrode of 2.1 mW/cm^2. The optical power mapping of the incident light and the transmitted light in the visible light range is shown in Figure S11. The response currents of the array elements are recorded immediately after the light is turned off (at 0 s), and again at 5 and 8 s post-exposure. The normalized current values, shown in Figure 6(d), indicate the temporal retention of the optical pattern, highlighting the memory effect of the device array. This experiment successfully validates the image recognition and retention capabilities of the ZnO/MoS_2 memristor array, demonstrating its applicability for neuromorphic visual perception systems.

Table 1 systematically summarizes the performance comparisons of the recently reported memristors with ZnO-based heterostructure as the functional layer. Notably, the ZnO/MoS_2 heterostructure memristor exhibits a much lower V_{set}, enhanced cyclic endurance, and extended retention time, which is beneficial to low-power storage and computing. Furthermore, the ZnO/MoS_2 heterostructure memristor has also demonstrated excellent optoelectronic modulation, promoting the development of the fields of sensing and neuromorphic computing.

3 Conclusion

This study experimentally demonstrated a ZnO/MoS_2-heterostructured dual-mode optoelectronic memristor and systematically investigated its resistive switching characteristics and synaptic emulation behaviors via electrical and optical stimuli. By inserting a MoS_2 isolation layer between the ZnO layer and the bottom electrode, the constructed ZnO/MoS_2 heterojunction memristor addresses the device instability resulting from the negative-SET behavior ob-

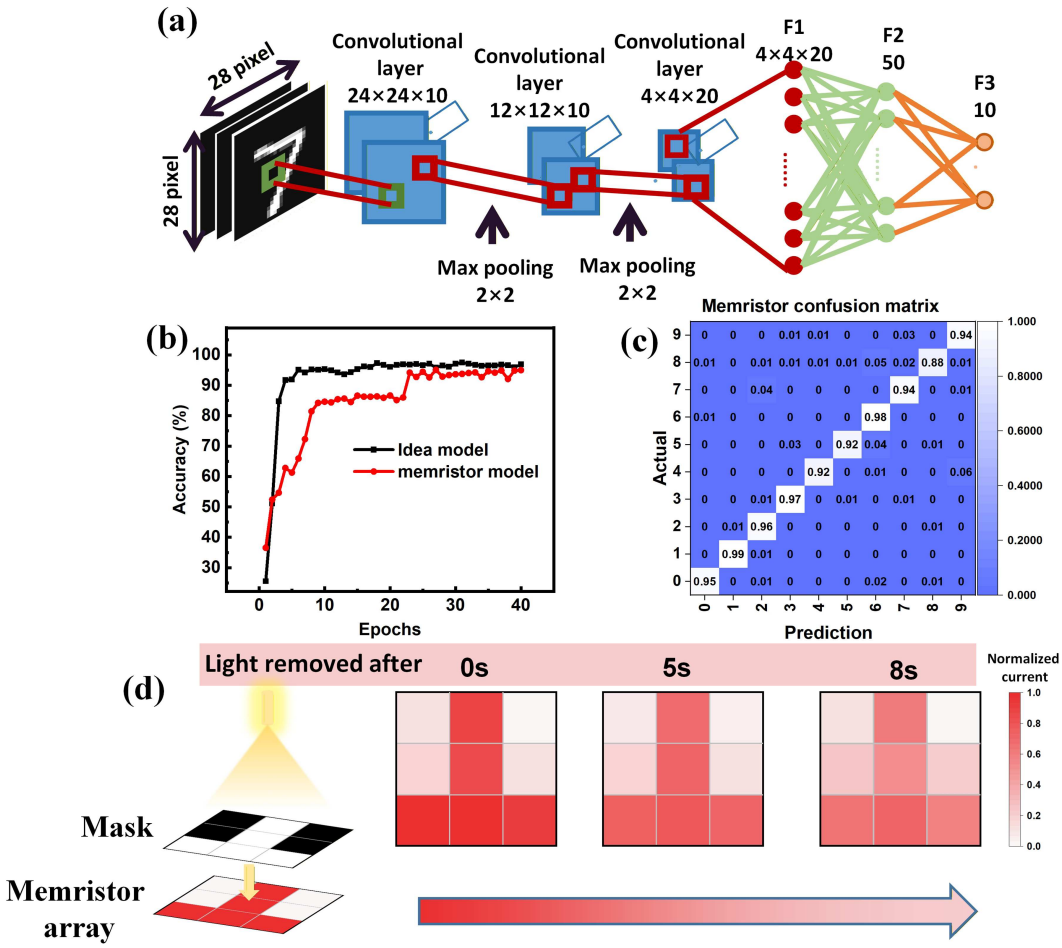

Figure 6 (Color online) (a) Schematic diagram of the simulated three-layer convolutional neural network structure; (b) evolution of accuracy with training epochs for the ZnO/MoS_2 memristor and compared to the ideal case; (c) confusion matrices showing the percentage of classification test of the MNIST; (d) normalized photocurrent image mapping of each unit in a 3×3 memristor array after removing light.

served in ZnO memristor and exhibits significantly enhanced operational stability, extended retention time, reduced switching voltage, enhanced uniformity, and accelerated response speed. Subsequently, first-principles calculations were conducted to elucidate the mechanism responsible for the performance enhancement in ZnO/MoS_2 heterojunction memristor, revealing that the MoS_2 layer effectively suppresses Ag^+ migration toward the Pt electrode under negative bias voltage, thereby inhibiting uncontrolled CF growth. Furthermore, typical biological synapse features, such as EPSC, SNDP, LTP, LTD, and PPF, were successfully reproduced by the ZnO/MoS_2 memristor under electrical and optical dual-mode operation. Based on the superior resistive switching characteristics and electrical/optical-stimuli synaptic plasticity, we employed SPICE simulations to implement memristor-based logic circuits that achieved AND, OR, and NOT functions. Leveraging ZnO/MoS_2 optoelectronic memristor as artificial synapses, a memristive CNN achieving 99% accuracy on MNIST digit classification (28×28 pixel) was implemented. In addition, a 3×3 ZnO/MoS_2 optoelectronic synapse array was developed to successfully simulate the human visual perception. The obtained results validate the capabilities of the proposed ZnO/MoS_2 optoelectronic synapse in in-memory computing and neuromorphic computing. This work provides a viable strategy for developing stable artificial synapses and bioinspired optoelectronic systems.

4 Experimental methods

Device fabrication: A 5 nm thick MoS_2 film was deposited on a clean Pt/Si substrate using a radio frequency (RF) magnetron sputtering at room temperature. The deposition process was maintained with an Ar gas flow of 2 sccm, 50 W power, and a working pressure of 2 mTorr. Hereafter, a 60 nm thick ZnO film was RF sputtered onto the MoS_2 film employing 100 W deposition power in Ar ambient at a flow rate of 50 sccm and a working pressure

of 5 mTorr at room temperature. Finally, a 100 nm Ag film and a 5 nm TiN film were sputtered on the ZnO film as the top electrode via DC magnetron sputtering with a shadow mask (DC power of 100 W and pressure of 1 mTorr).

Characterization and measurement: The SEM images and element distribution characterization of the ZnO/MoS_2 memristor were performed using Hitachi Regulus 8100. XRD patterns were performed by Rigaku Ultima IV. The transmission and absorption spectra were recorded by an ultraviolet and visible (UV-vis) spectrum analyzer (PerkinElmer Lamda35). The I-V characteristics of the device were measured by the semiconductor parameter analyzer (Keithley 4200A-SCS) in the probe station.

Acknowledgements This work was supported by National Key R&D Program of China (Grant No. 2023YFB3610500), National Natural Science Foundation of China (Grant Nos. 62204128, 62404112, 62471251), Natural Science Foundation of Jiangsu Province (Grant Nos. BK20220399, BK20243037, BK20240033, BK20245037), Foundation of Jiangsu Provincial Double-Innovation Doctor Program (Grant No. JSSCBS20210522), Natural Science Foundation of Nanjing University of Posts and Telecommunications (Grant Nos. NY223158, NY224078, NY222178, NY224140, NY224056), and Industry-University Collaborative Project (Grant Nos. 2022out212, 2024out026, 2024out254).

Supporting information Figures S1–S11, Table S1, and Appendixes A–C. The supporting information is available online at info.scichina.com and link.springer.com. The supporting materials are published as submitted, without typesetting or editing. The responsibility for scientific accuracy and content remains entirely with the authors.

References

1 Yang J J, Strukov D B, Stewart D R. Memristive devices for computing. Nat Nanotechnol, 2013, 8: 13–24
2 Feng Y, Zhang Y, Zhou Z, et al. Memristor-based storage system with convolutional autoencoder-based image compression network. Nat Commun, 2024, 15: 1132
3 Liu Z, Mei J, Tang J, et al. A memristor-based adaptive neuromorphic decoder for brain-computer interfaces. Nat Electron, 2025, 8: 362–372
4 Yi S i, Kendall J D, Williams R S, et al. Activity-difference training of deep neural networks using memristor crossbars. Nat Electron, 2023, 6: 45–51
5 Jain S, Li S, Zheng H, et al. Heterogeneous integration of 2D memristor arrays and silicon selectors for compute-in-memory hardware in convolutional neural networks. Nat Commun, 2025, 16: 2719
6 Shi T, Gao L, Tian Y, et al. Memristor-based feature learning for pattern classification. Nat Commun, 2025, 16: 913
7 Li M, Li C, Ye K, et al. Self-powered photonic synapses with rapid optical erasing ability for neuromorphic visual perception. Research, 2024, 7: 526
8 Yuan R, Tiw P J, Cai L, et al. A neuromorphic physiological signal processing system based on VO2 memristor for next-generation human-machine interface. Nat Commun, 2023, 14: 3695
9 Li Y, Tang J, Gao B, et al. Monolithic three-dimensional integration of RRAM-based hybrid memory architecture for one-shot learning. Nat Commun, 2023, 14: 7140
10 Kim M, Ducournau G, Skrzypczak S, et al. Monolayer molybdenum disulfide switches for 6G communication systems. Nat Electron, 2022, 5: 367–373
11 Park S O, Jeong H, Park J, et al. Experimental demonstration of highly reliable dynamic memristor for artificial neuron and neuromorphic computing. Nat Commun, 2022, 13: 2888
12 Khwa W S, Wen T H, Hsu H H, et al. A mixed-precision memristor and SRAM compute-in-memory AI processor. Nature, 2025, 639: 617–623
13 Song M, Liu N, Zhou S, et al. A design of 2-stage voltage ramp-up SRAM physical unclonable function. Chin J Elect, 2024, 33: 371–379
14 Yan T, Cai Y C, Wang Y R, et al. Near-infrared optoelectronic synapses based on a Te/α-In_2Se_3 heterojunction for neuromorphic computing. Sci China Inf Sci, 2023, 66: 160404
15 Han J Q, Li Z Z, Zeng T, et al. Multi-wavelength plasmonic optoelectronic memristor for reconfigurable logic operations and mixed-color pattern recognition. Sci China Inf Sci, 2025, 68: 120401
16 Cheng X, Dou Z, Lian H, et al. Principles, fabrication, and applications of halide perovskites-based memristors. FlexMat, 2024, 1: 127–149
17 Wei B, Chen Y B, Han X T, et al. Ultra-low power MoS_2 optoelectronic synapse with wavelength sensitivity for color target recognition. Sci Chi Inf Sci, 2025, 68: 140406
18 Mao Q, Zhu Z, Meng J, et al. Intelligent flexible memristors for artificial synapses and neuromorphic computing. FlexMat, 2025, 2: 188–203
19 Huang F, Sun X, Shi Y, et al. Flexible ionic-gel synapse devices and their applications in neuromorphic system. FlexMat, 2025, 2: 30–54
20 Li L, Li Y, Luo B, et al. Preparation and thermal properties of bionic nacre composite materials based on exfoliated montmorillonite. J Mater Sci-Mater Electron, 2023, 34: 93–103
21 Chen J, Liu X, Liu C, et al. Reconfigurable Ag/HfO_2/NiO/Pt memristors with stable synchronous synaptic and neuronal functions for renewable homogeneous neuromorphic computing system. Nano Lett, 2024, 24: 5371–5378
22 Huang H, Liang X, Wang Y, et al. Fully integrated multi-mode optoelectronic memristor array for diversified in-sensor computing. Nat Nanotechnol, 2025, 20: 93–103
23 Wu Y, Wei Y, Huang Y, et al. Capping $CsPbBr_3$ with ZnO to improve performance and stability of perovskite memristors. Nano Res, 2017, 10: 1584–1594
24 Wang W, Li K, Lan J, et al. CMOS backend-of-line compatible memory array and logic circuitries enabled by high performance atomic layer deposited ZnO thin-film transistor. Nat Commun, 2023, 14: 6079

25 Zhou Z, Pei Y, Zhao J, et al. Visible light responsive optoelectronic memristor device based on CeO_x/ZnO structure for artificial vision system. Appl Phys Lett, 2021, 118: 191103

26 Zheng J, Du Y, Dong Y, et al. Fully light-modulated memristor based on ZnO/MoO_x heterojunction for neuromorphic computing. Appl Phys Lett, 2024, 124: 133502

27 Lin Q, Zhu Y, Sun J, et al. A full-quantum-dot optoelectronic memristor for in-sensor reservoir computing system with integrated functions. Adv Funct Mater, 2025, 35: 2423548

28 Li X, Fang Z, Guo X, et al. Light-induced conductance potentiation and depression in an all-optically controlled memristor. ACS Appl Mater Interfaces, 2024, 16: 27866–27874

29 Wang X, Guo Z, Zheng W, et al. Resistive switching behaviors and conduction mechanisms of IGZO/ZnO bilayer heterostructure memristors. APL Mater, 2024, 12: 111105

30 Wang W, Li Y, Yue W, et al. Study on multilevel resistive switching behavior with tunable ON/OFF ratio capability in forming-free ZnO QDs-based RRAM. IEEE Trans Electron Devices, 2020, 67: 4884–4890

31 Ghafoor F, Kim H, Ghafoor B, et al. Interface engineering in ZnO/CdO hybrid nanocomposites to enhanced resistive switching memory for neuromorphic computing. J Colloid Interface Sci, 2024, 659: 1–10

32 Patil H, Kim H, Rehman S, et al. Stable and multilevel data storage resistive switching of organic bulk heterojunction. Nanomaterials, 2021, 11: 359

33 Xu L, Wang W, Li Y, et al. N:ZnO/MoS_2-heterostructured flexible synaptic devices enabling optoelectronic co-modulation for robust artificial visual systems. Nano Res, 2024, 17: 1902–1912

34 Wu F, Si S, Cao P, et al. Interface engineering via MoS_2 insertion layer for improving resistive switching of conductive-bridging random access memory. Adv Elect Mater, 2019, 5: 1800747

35 Gautam C, Verma A, Chaudhary P, et al. Development of 2D based ZnO-MoS_2 nanocomposite for photodetector with light-induced current study. Optical Mater, 2022, 123: 111860

36 Liu H Q, Yao C B, Liu X J, et al. Heterointerface-enhanced ultrafast carrier dynamics and nonlinear optical response via constructing electronic structure-induced type-I ZnO-MoS_2 n-n heterojunction. Appl Surf Sci, 2022, 580: 152222

37 Kumawat K L, Augustine P, Singh D K, et al. Electrically modulated wavelength-selective photodetection enabled by MoS_2/ZnO heterostructure. Phys Rev Appl, 2022, 17: 064036

38 Qian C X, Deng Z Y, Yang K, et al. Interface engineering of $CsPbBr_3/TiO_2$ heterostructure with enhanced optoelectronic properties for all-inorganic perovskite solar cells. Appl Phys Lett, 2018, 112: 093901

39 Huang C H, Huang J S, Lin S M, et al. ZnO_{1-x} nanorod arrays/ZnO thin film bilayer structure: from homojunction diode and high-performance memristor to complementary 1D1R application. ACS Nano, 2012, 6: 8407–8414

40 Jiang S, Peng L, Hao Z, et al. Self-powered organic optoelectronic synapses with binarized weights for noise-suppressed visual perception and high-robustness inference. ACS Appl Electron Mater, 2023, 5: 4915–4924